

Critical behavior in the itinerant ferromagnet $SmMn_2Ge_2$

Qingyi Hou(侯清漪), Meng Song(宋猛), Xitong Xu(许锡童), Yihao Wang(王宜豪), Chao Dong(董超),Yinfa Feng(冯寅发), Miao He(何苗), Yonglai Liu(刘永来), Liang Cao(曹亮), Junfeng Wang(王俊峰),Zhe Qu(屈哲), and Yimin Xiong(熊奕敏)

Citation: Chin. Phys. B, 2023, 32 (**8**): 087501. DOI: 10.1088/1674-1056/accb49
Journal homepage: http://cpb.iphy.ac.cn; http://iopscience.iop.org/cpb

What follows is a list of articles you may be interested in

Critical behavior and effect of Sr substitution in double perovskite Ca_2CrSbO_6

Yuan-Yuan Jiao(焦媛媛), Jian-Ping Sun(孙建平), and Qi Cui(崔琦)
Chin. Phys. B, 2021, 30 (**3**): 037501. DOI: 10.1088/1674-1056/abc67b

Critical behavior in the layered organic-inorganic hybrid $(CH_3NH_3)_2CuCl_4$

Tina Raoufi, Yinina Ma(马怡妮娜), Young Sun(孙阳)
Chin. Phys. B, 2020, 29 (**6**): 067503. DOI: 10.1088/1674-1056/ab892c

Magnetocaloric effect and critical behavior of the Mn-rich itinerant material Mn_3GaC with enhanced ferromagnetic interaction

Pengfei Liu(刘鹏飞), Jie Peng(彭杰), Mianqi Xue(薛面起), Bosen Wang(王铂森)
Chin. Phys. B, 2020, 29 (**4**): 047503. DOI: 10.1088/1674-1056/ab7da1

Critical behavior and magnetocaloric effect in magnetic Weyl semimetal candidate $Co_{2-x}ZrSn$

Tianlin Yu(于天麟), Xiaoyun Yu(余骁昀), En Yang(杨恩), Chang Sun(孙畅), Xiao Zhang(张晓), Ming Lei(雷鸣)
Chin. Phys. B, 2019, 28 (**6**): 067501. DOI: 10.1088/1674-1056/28/6/067501

Computational study of inverse ferrite spinels

A EL Maazouzi, R Masrour, A Jabar, M Hamedoun
Chin. Phys. B, 2019, 28 (**5**): 057504. DOI: 10.1088/1674-1056/28/5/057504

Critical behavior in the itinerant ferromagnet $SmMn_2Ge_2$

Qingyi Hou(侯清漪)[1,2,†], Meng Song(宋猛)[1,2,†], Xitong Xu(许锡童)[1], Yihao Wang(王宜豪)[1], Chao Dong(董超)[3], Yinfa Feng(冯寅发)[3], Miao He(何苗)[1,2], Yonglai Liu(刘永来)[1,2], Liang Cao(曹亮)[1], Junfeng Wang(王俊峰)[3], Zhe Qu(屈哲)[1,2,‡], and Yimin Xiong(熊奕敏)[4,5,§]

[1] *Anhui Province Key Laboratory of Condensed Matter Physics at Extreme Conditions, CAS Key Laboratory of Photovoltaic and Energy Conservation Materials, High Magnetic Field Laboratory of Chinese Academy of Sciences (CHMFL), HFIPS, Chinese Academy of Sciences, Hefei* 230031, *China*

[2] *Science Island Branch of Graduate School, University of Science and Technology of China, Hefei* 230026, *China*

[3] *Wuhan National High Magnetic Field Center and School of Physics, Huazhong University of Science and Technology, Wuhan* 430074, *China*

[4] *Department of Physics, School of Physics and Optoelectronics Engineering, Anhui University, Hefei* 230601, *China*

[5] *Hefei National Laboratory, Hefei* 230028, *China*

(Received 11 February 2023; revised manuscript received 23 March 2023; accepted manuscript online 7 April 2023)

Transition metal and rare earth intermetallics have been a fertile playground for research of various quantum states. We report detailed magnetic studies on $SmMn_2Ge_2$, an anisotropic itinerant magnet with multiple magnetic phases. The critical behavior of the ferromagnetic phase transition is investigated by employing the modified Arrott plot with the Kouvel–Fisher method. The critical temperature T_c is determined to be around 342.7 K with critical exponents of $\beta = 0.417$ and $\gamma = 1.122$, and the interaction function is found to be $J(r) \sim r^{-4.68}$, suggesting the coexistence of long-range and short-range magnetic interactions. Our results contribute to the understanding of complex magnetism in $SmMn_2Ge_2$, which may provide fundamental guidance in future spintronic applications.

Keywords: critical exponent, itinerant ferromagnet, rare earth

PACS: 75.40.Cx, 75.20.En, 75.30.Gw **DOI:** 10.1088/1674-1056/accb49

1. Introduction

Ternary rare-earth compounds RT_2X_2 (R = rare-earth elements, T = transition metals, and X = Ge, Si) have attracted much attention in recent years due to their strong spin–orbit coupling, enhanced Coulomb interaction, and electron correlation. Combined with the partially filled 3d and 4f electron orbitals, this family can host abundant physical properties including heavy fermion behavior, quantum criticality, unconventional superconductivity, and novel magnetism.[1–4] Among them, the RMn_2Ge_2 compounds crystallize in a layered $ThCr_2Si_2$-type tetragonal structure with space group $I4/mmm$, and have a particularly attractive nature due to the relatively large magnetic moment of Mn ions. The atoms lie on the alternate layers stacked along the c-axis with a sequence of R–Ge–Mn–Ge–R, as shown in Fig. 1(a). In RMn_2Ge_2 compounds, owing to the coexistence of exchange interactions between the localized moments, interband Kondo interaction, and Ruderman–Kittel–Kasuya–Yosida (RKKY) interaction, abundant and novel magnetic phases have been observed.[5] Recent works also reported the topological magnetic texture of room-temperature stable skyrmion bubbles and giant topological Hall effect in RMn_2Ge_2 (R = Ce, Pr, and Nd) compounds owing to the noncollinear/noncoplanar spin structures.[6–8]

In RMn_2Ge_2 compounds, the interlayer Mn–Mn coupling is controlled by the intralayer Mn–Mn distance, with antiferromagnetic (AFM) coupling for $R^a_{Mn-Mn} < 2.85$ Å and ferromagnetic (FM) for $R^a_{Mn-Mn} > 2.85$ Å. $SmMn_2Ge_2$ happens to possess this critical distance, and undergoes a series of magnetic phase transitions as temperature changes.[9] Extensive investigations have been performed on this compound to figure out its magnetic structures in the entire temperature range. $SmMn_2Ge_2$ undergoes a paramagnetic (PM) to FM transition at $T_C \sim 350$ K, and an FM-to-AFM phase transition at T_{t1} (~ 150 K), both transitions dominated by the magnetic coupling of Mn sublattice. In the FM region, the Mn moments are AFM-coupled within the ab plane whereas FM-coupled along the c direction. In the AFM region, the coupling along the c direction is also AFM due to the decrease of intralayer Mn–Mn distance. For even lower temperature (below $T_{t2} \sim 100$ K), the moments of Sm become FM coupled along the a direction which dominates over the Mn–Mn coupling, and $SmMn_2Ge_2$ is in a re-entrant ferromagnetic (RFM) phase.[10] These make $SmMn_2Ge_2$ a proper specimen to study the underlying mechanism of the various magnetic phases. In this work, we report critical behavior studies on $SmMn_2Ge_2$ and identify this material as an itinerant ferromagnet with multiple-range magnetic interactions by the large Rhodes–Wohlfarth (RW) ratio (~ 3.20) and interaction function $J(r) \sim r^{-4.68}$.

[†] Qingyi Hou and Meng Song contributed equally to this work.

[‡] Corresponding author. E-mail: zhequ@hmfl.ac.cn

[§] Corresponding author. E-mail: yxiong@ahu.edu.cn

© 2023 Chinese Physical Society and IOP Publishing Ltd

2. Methods

Single crystals of $SmMn_2Ge_2$ were synthesized by using In-flux with a molar ratio of Sm : Mn : Ge : In = 1.05 : 2 : 2 : 30. Sm powder, Mn powder, Ge powder, and In grains were mixed and placed in an alumina crucible, the mixture was then sealed in an evacuated quartz tube to avoid oxidation. The tube was placed in a furnace and kept at 1060 °C for one day to obtain a homogeneous metallic solution, and then cooled to 700 °C at a rate of 3 °C/h and kept at 700 °C for another day to minimize potential crystal defects. To isolate individual single crystals, the quartz tube was rapidly transferred to a centrifuge to remove excessive In flux at 700 °C. The isothermal magnetization up to 50 T was measured in a pulsed magnetic field at Wuhan National High Magnetic Field Center.

3. Results

Figure 1(b) shows the x-ray diffraction (XRD) pattern of $SmMn_2Ge_2$ single crystal. The sharp rocking curve in the inset indicates good crystallization quality. In Fig. 1(c), the temperature dependence of the magnetic susceptibility is shown for magnetic field $\mu_0 H = 0.02$ T along the *ab*-plane and *c*-axis. Multiple magnetic phase transitions are observed as the temperature changes, including an FM transition at $T_C \sim 343$ K, an FM-to-AFM transition at $T_{t1} \sim 150$ K, and an RFM transition at $T_{t2} \sim 100$ K. Obvious magnetic anisotropy is observed in both high-temperature FM and low-temperature RFM phases. In the high-temperature FM phase, the long-range magnetic ordering is determined by FM coupling between Mn–Mn moments, which are oriented to the *c* direction. There is also an AFM component in the *ab*-plane that has nearly equal strength compared to the FM component. As a result, the susceptibility χ_c is relatively larger than χ_{ab} at low field. In the RFM phase below 100 K, the in-plane FM coupling between Sm–Sm is dominant, leading to a net in-plane FM coupling with an AFM component along the *c*-axis.[11] Consequently, a χ_{ab} much larger than χ_c is observed.

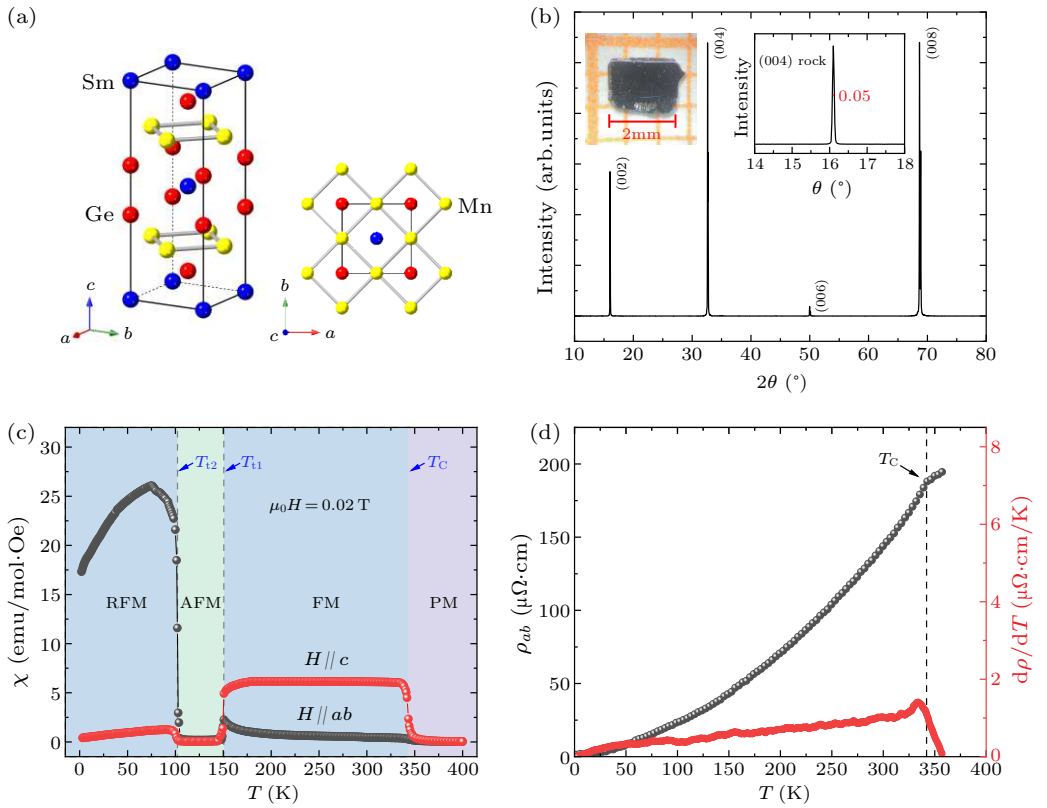


Fig. 1. (a) Side view (left) and top view (right) of $SmMn_2Ge_2$ crystal structure. (b) XRD pattern of $SmMn_2Ge_2$ single crystal. The left inset shows a typical $SmMn_2Ge_2$ single crystal. The right inset shows the rocking curve of (004) reflection. (c) Temperature dependence of magnetic susceptibility under zero-field-cooling and an applied field of 0.02 T. PM: paramagnetic, FM: ferromagnetic, AFM: antiferromagnetic, RFM: re-entrant ferromagnetic. (d) In-plane resistivity ρ_{ab} and $d\rho/dT$ as a function of temperature.

In the temperature range of 360–400 K, the magnetic susceptibility $\chi(T)$ can be well fitted by the modified Curie–Weiss law

$$\chi(T) = \chi_0 + \frac{C}{T - \theta_p}, \tag{1}$$

where χ_0 is a temperature-independent contribution, C is the Curie constant, and θ_p is the Weiss temperature. The fitting results are summarized in Table 1. The effective magnetic moments for $H // ab$ and $H // c$ are 3.15 μ_B/Mn and 3.52 μ_B/Mn, respectively, which are slightly smaller than the theoretical value 3.82 μ_B of Mn^{3+} ion due to the canted spin.[12] The Rhodes–Wohlfarth (RW) ratio q_c/q_s reflects the change in the

number of the magnetic carrier with temperature, and can be used as a criterion for identifying itinerant magnets. Here, q_c is estimated from the effective moment ($\mu_{eff}^2 = q_c(q_c+2)\mu_B^2$) and q_s is calculated from the saturated moment ($\mu_{sat} = 2q_s\mu_B$) at 200 K.[13] The RW ratios for H // ab and H // c are 2.83 and 3.20, respectively, indicating that the $SmMn_2Ge_2$ is an itinerant magnet.

In the ρ_{ab} versus T curve (Fig. 1(d)), a kink was seen at the ferromagnetic transition temperature $T_C \sim 343$ K, due to a significant change of spin scattering. However, no clear signatures of other magnetic transitions could be observed in the resistivity and the $d\rho/dT$ curve.

It is known that the magnetic structure of $SmMn_2Ge_2$ single crystal is strongly anisotropic.[14] As shown in Fig. 2(a), below $T_{t2} \sim 100$ K, a large bifurcation is observed between the zero-field-cooling (ZFC) and field-cooling (FC) curves under a low magnetic field in the ab-plane, indicating a considerable effect of the FM domains. However, a much smaller bifurcation is observed when the applied field is along the c-axis, as shown in Fig. 2(b), suggesting an external field orientation controlled magnetic domain texture in our sample. With the increase of the external field, both RFM and FM to AFM transitions were suppressed by a field of 4 T. At 4 T, the magnetization in the ab-plane shows an FM-like temperature dependence (see Fig. 2(a)), suggesting that the in-plane FM interactions induced by Sm–Sm coupling can be enhanced by applied field and has pronounced effects at temperatures above RFM transition temperature T_{t2}. Moreover, the AFM transition is strongly suppressed under the 4 T field along the c-axis (see Fig. 2(b)), while it still represents a strong AFM component along the c direction.

Figures 2(c) and 2(d) show M versus H under the external field in the ab-plane and along the c-axis at selected temperatures. Below T_C, the M versus H curves show the FM behavior generally. Notably, a metamagnetic transition is observed in the curves measured at 125 K under both field directions as shown in the insets of Figs. 2(c) and 2(d). With decreasing temperature, the system enters an RFM state induced by Sm–Sm coupling after a first-order FM transition at ~ 100 K, which has been reported in the literature on $SmMn_2Ge_2$.[14]

Table 1. The fitting parameters of modified Curie–Weiss law and RW ratios for $SmMn_2Ge_2$.

Field direction	Fitting range (K)	χ_0 (10^{-3} emu/mol)	C (emu·K/mol)	θ_p (K)	μ_{eff} (μ_B/Mn)	RW
H // ab	$360 \leqslant T \leqslant 400$	1.47	2.48	334.72	3.15	2.83
H // c	$360 \leqslant T \leqslant 400$	−11.91	3.10	344.82	3.52	3.20

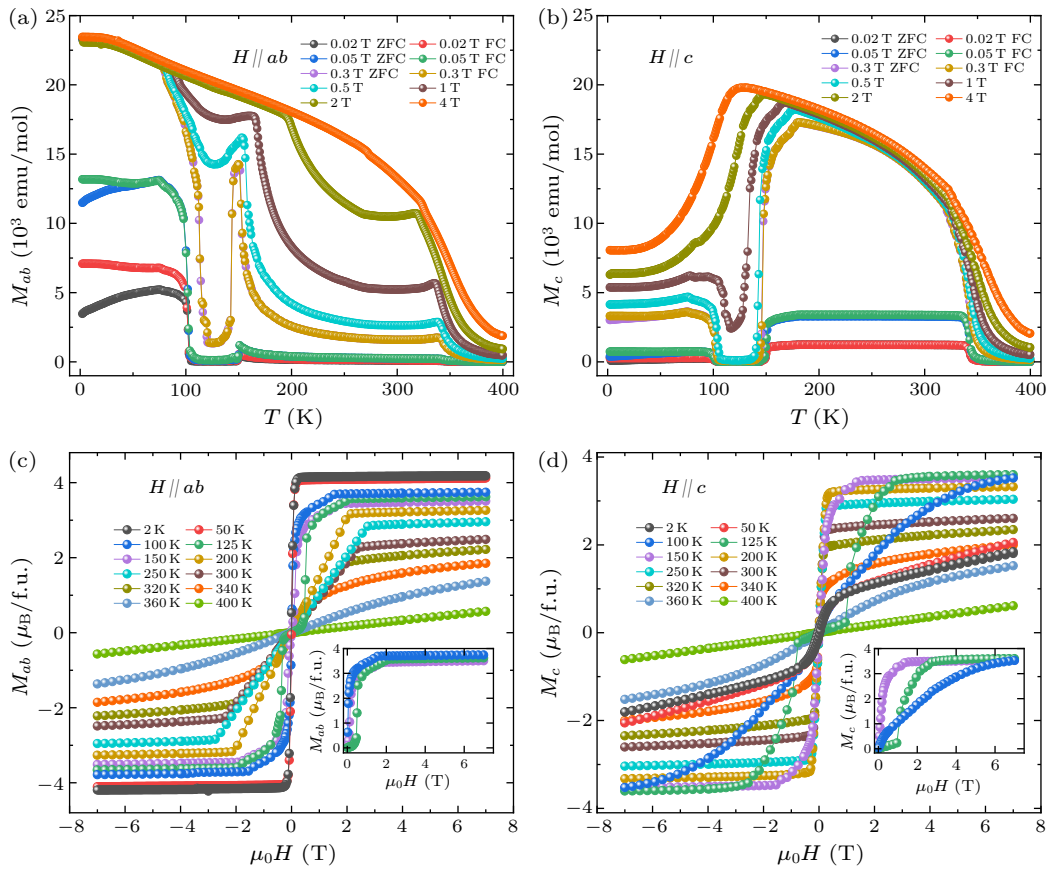


Fig. 2. Temperature dependence of magnetization with field along (a) ab-plane and (b) c-axis. Magnetic field dependence of magnetization with field along (c) ab-plane and (d) c-axis.

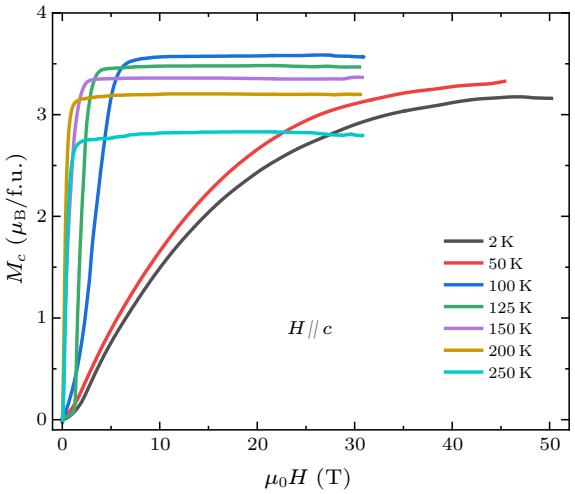


Fig. 3. The isothermal magnetization measured in a high pulsed magnetic field at representative temperatures for $H // c$.

In addition, to fully magnetize $SmMn_2Ge_2$ along the c axis, pulsed-field magnetization measurements were carried out. As shown in Fig. 3, a magnetic field of 10 T along the c direction is sufficient to fully polarize the magnetization above 100 K. Due to the strong in-plane FM Sm–Sm and Sm–Mn coupling, for temperature below 50 K, the saturation field is higher than 40 T.

The analysis of critical behavior and critical exponent can reflect the dimensionality, coherence length, and correlation distance of spins. Consequently, it can effectively reveal the interaction and coupling mechanism of a magnetically ordered system.[15] For several RMn_2Ge_2 compounds, the topological spin textures have been observed around room temperature due to competition between long-range and short-range magnetic interactions.[7,8] Here, to understand the magnetic interactions and ground state of Mn–Mn magnetic coupling in $SmMn_2Ge_2$, the critical behavior analysis around $T_C \sim 343$ K has been performed. The isothermal field dependence magnetization for $H // ab$ in the temperature range from 330 K to 360 K with steps of $\Delta T = 1$ K was measured and plotted in Fig. 4(a). Arrott plots for the mean field model and the modified Arrott plots (MAPs) for universal models: 3D-Heisenberg, 3D-XY, 3D-Ising, and tricritical mean field are plotted in Figs. 4(b)–4(f), respectively. The corresponding critical exponents are listed in Table 2 for comparison. According to the Arrott–Noakes equation, the MAPs near the critical temperature should display parallel lines in high field region with suitable critical exponents.[16] By defining the normalized slope $NS = S(T)/S(T_C)$, where $S(T)$ represents the high field slope of the MAPs at temperature T, we can judge whether the critical exponents are suitable. For the ideal case, the normalized slope NS should remain constant with temperature and equal to 1. Figure 5(a) shows the NS values of different models as a function of temperature. It can be seen that none of the models meet the above conditions, indicating that the critical behavior of $SmMn_2Ge_2$ does not belong to a single universality class.

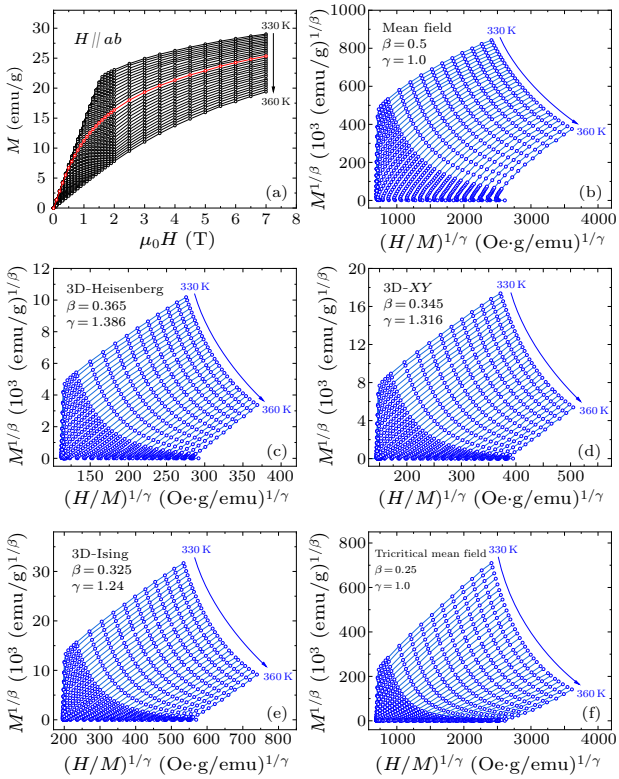


Fig. 4. (a) Isothermal field dependence magnetization curves measured at $H // ab$ in the temperature range from 330 K to 360 K with steps of $\Delta T = 1$ K. (b) Arrott plot of $SmMn_2Ge_2$ for mean field theory. Modified Arrott plot of $M^{1/\beta}$ vs. $(H/M)^{1/\gamma}$ for (c) the 3D-Heisenberg model, (d) 3D-XY model, (e) 3D-Ising model, and (f) tricritical mean field model.

For a second-order magnetic phase transition, the critical exponents can be obtained by the following equations:[17,18]

$$M_S(T) = M_0(-\varepsilon)^{\beta}, \quad \varepsilon < 0,\ T < T_C, \tag{2a}$$

$$\chi_0^{-1}(T) = (h_0/M_0)\varepsilon^{\gamma}, \quad \varepsilon > 0,\ T > T_C, \tag{2b}$$

$$M = DH^{1/\delta}, \quad \varepsilon = 0,\ T = T_C, \tag{2c}$$

where M_0, h_0/M_0, and D are the critical amplitudes, and the $\varepsilon = (T - T_C)/T_C$ is the reduced temperature.

The initial critical exponents can be obtained from the magnetic field dependent magnetization and magnetic entropy change curves around T_C, where the magnetic entropy change has an exponential relationship with the magnetic field, $-\Delta S_M^{max} \propto H^n$.[19] The magnetic entropy change is defined as[20]

$$\Delta S_M(T,H) = \int_0^H \left[\frac{\partial M(T,H)}{\partial T}\right]_H \mathrm{d}H. \tag{3}$$

Figure 5(b) exhibits the temperature dependence of magnetic entropy change curves at 330 K–360 K. By fitting the magnetic entropy change curve at 343 K, $n = 0.503$ is obtained, as shown in the inset of Fig. 5(b). This exponent n has a universal relation with β and γ,[19]

$$n = 1 + \frac{\beta - 1}{\beta + \gamma}. \tag{4}$$

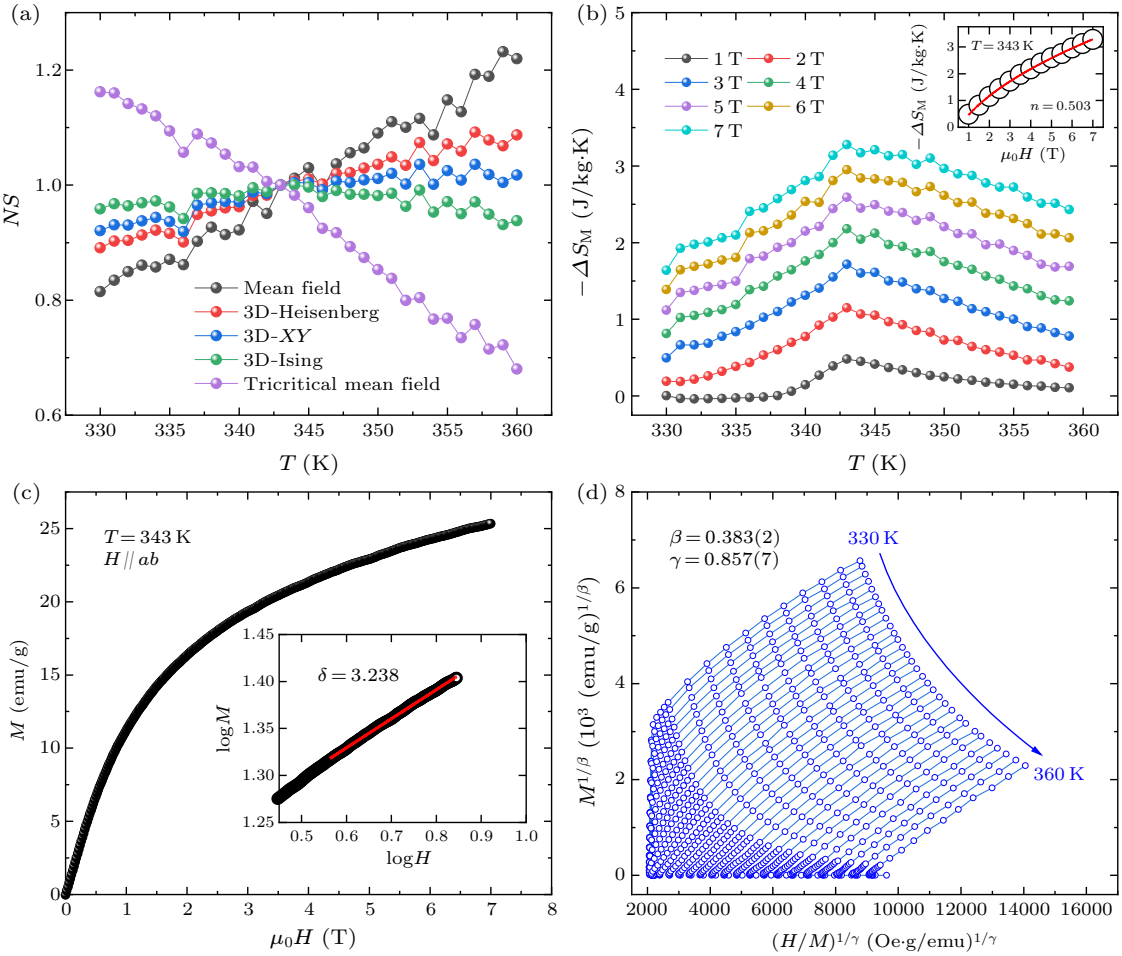


Fig. 5. (a) Temperature dependence of the normalized slope (*NS*). (b) Temperature dependence of the magnetic entropy change $-\Delta S_{\rm M}$. Inset: field dependence of the magnetic entropy change $-\Delta S_{\rm M}$ at 343 K. (c) Field dependence of magnetization at $T_{\rm C} = 343$ K. Inset: the fitting curve of log*M*–log*H* by using Eq. (2c). (d) Modified Arrott plot of $M^{1/\beta}$ vs. $(H/M)^{1/\gamma}$ with $\beta = 0.383(2)$ and $\gamma = 0.857(7)$.

Table 2. Comparison of the critical exponents of the $SmMn_2Ge_2$ single crystal with the theoretical models.

Composition	Technique	β	γ	δ	$T_{\rm C}$ (K)	
3D-Heisenberg	theory	0.365	1.386	4.8	—	Ref. [23]
3D-*XY*	theory	0.345	1.316	4.81	—	Ref. [23]
3D-Ising	theory	0.325	1.24	4.82	—	Ref. [23]
Tricritical mean field	theory	0.25	1.0	5.0	—	Ref. [24]
Mean field	theory	0.5	1.0	3.0	—	Ref. [24]
$SmMn_2Ge_2$	MAP	0.417(6)	1.122(9)	3.688(9)	342.7	this work
$SmMn_2Ge_2$	KF	0.419(8)	1.131(9)	3.696(2)	342.7	this work

Figure 5(c) shows the magnetic field dependence of the magnetization curve at $T_{\rm C} = 343$ K, and its inset exhibits the log–log plot of the data in the high field region. By the linear fit, $\delta = 3.238$ is estimated based on Eq. (2c). In addition, according to Widom's scaling theory, the critical exponents of β, γ, and δ are related in the following way:[21]

$$\delta = 1 + \frac{\gamma}{\beta}. \tag{5}$$

From the n and δ obtained above, the initial critical exponents are calculated as $\beta = 0.383(2)$, $\gamma = 0.857(7)$, $\delta = 3.238$, and a new MAP is constructed in Fig. 5(d).

By fitting the new MAP, a set of convergent critical exponents are finally obtained as $\beta = 0.417(6)$ with $T_{\rm C} = 342.71(2)$ K and $\gamma = 1.122(9)$ with $T_{\rm C} = 342.50(3)$ K, as shown in Fig. 6(a). Meanwhile, the critical exponents can also be obtained by using the Kouvel–Fisher (KF) method,[22]

$$\frac{M_{\rm S}(T)}{{\rm d}M_{\rm S}(T)/{\rm d}T} = \frac{T - T_{\rm C}}{\beta}, \tag{6a}$$

$$\frac{\chi_0^{-1}(T)}{{\rm d}\chi_0^{-1}(T)/{\rm d}T} = \frac{T - T_{\rm C}}{\gamma}. \tag{6b}$$

According to this method, the linear fits in Fig. 6(b) yield $\beta = 0.419(8)$ with $T_{\rm C} = 342.73(7)$ K, and $\gamma = 1.131(9)$ with $T_{\rm C} = 342.45(4)$ K, which is very close to the values obtained from the MAP method, indicating that the obtained critical exponents are reliable.

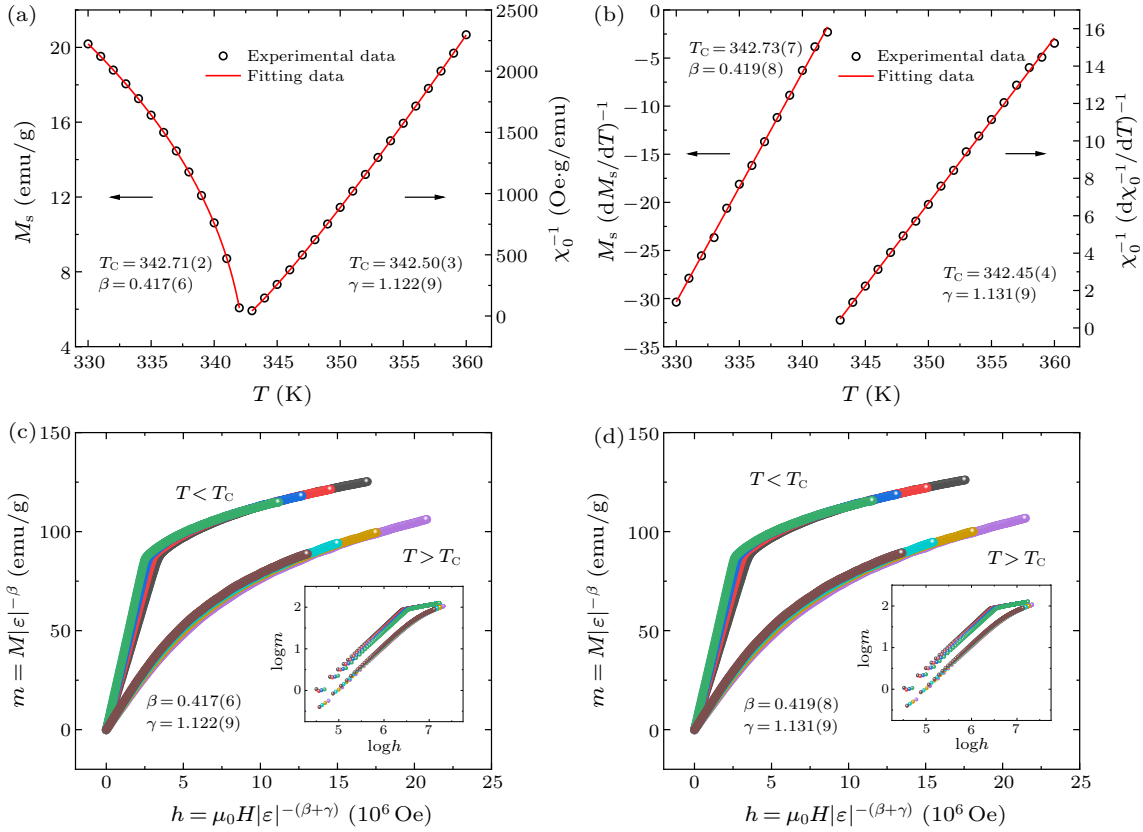


Fig. 6. (a) Temperature dependence of the spontaneous magnetization M_S (left) and the inverse initial susceptibility χ_0^{-1} (right), which are fitted by using Eqs. (2a) and (2b). (b) Kouvel–Fisher plots of $M_S(T)/[\mathrm{d}M_S(T)/\mathrm{d}T]$ (left) and $\chi_0^{-1}(T)/[\mathrm{d}\chi_0^{-1}(T)/\mathrm{d}T]$ (right) vs. T. The β, γ, and T_C are obtained from the linear fits by using Eqs. (6a) and (6b). (c) Scaling plots of renormalized magnetization m vs. renormalized field h below and above T_C with $\beta = 0.417(6)$ and $\gamma = 1.122(9)$. (d) Scaling plots of renormalized magnetization m vs. renormalized field h below and above T_C with $\beta = 0.419(8)$ and $\gamma = 1.131(9)$.

Moreover, the critical exponents can be examined by rescaling the isothermal magnetization.[17] As shown in Figs. 6(c) and 6(d), the data below and above T_C are collapsed into two separate branches. These well-renormalized isothermal magnetization curves further reveal that the critical exponents β, γ, and T_C are intrinsic and reliable. The parameters of theoretical models and the critical exponents obtained in our work are listed in Table 2.

The critical exponents obtained in this work, especially for β and γ, are in between the long-range mean field model and short-range 3D magnetic models, suggesting the coexistence of long-range and short-range magnetic interactions in $SmMn_2Ge_2$. For a homogeneous magnetic system, the attenuation distance J of the spin interaction determines the universality of magnetic phase transition. Fisher *et al.* theoretically treated this interaction as two spins attracting each other. According to the renormalization group theory, the interaction intensity $J(r)$ decays with the increasing spatial distance r,[25]

$$J(r) \sim r^{-(d+\sigma)}, \tag{7}$$

where d is the spatial dimensionality and σ is a position constant. We can obtain σ using the following equation:[25]

$$\gamma = 1 + \frac{4}{d}\left(\frac{n+2}{n+8}\right)\Delta\sigma + \frac{8(n+2)(n-4)}{d^2(n+8)^2} \times \left[1 + \frac{2G\left(\frac{d}{2}\right)(7n+20)}{(n-4)(n+8)}\right]\Delta\sigma^2, \tag{8}$$

where $\Delta\sigma = \sigma - \frac{d}{2}$, $G\left(\frac{d}{2}\right) = 3 - \frac{1}{4}\left(\frac{d}{2}\right)^2$, and n is the spin dimensionality. For $SmMn_2Ge_2$ we obtain $\sigma = 1.68$ and the interaction function $J(r) \sim r^{-4.68}$. This value of σ is larger than the long-range interaction one ~ 1.5, but smaller than that of short-range interaction ~ 2.0, further demonstrating the effect of multiple-range magnetic interactions. This is consistent with previous findings in $LaMn_2Ge_2$[26] and $PrMn_2Ge_2$,[27] and provides a reasonable theoretical explanation for the noncollinear spin structure and observation of topological skyrmion bubbles in such compounds, e.g., $PrMn_2Ge_2$, $NdMn_2Ge_2$, and $CeMn_2Ge_2$.[6]

4. Conclusion

In summary, we have analyzed the critical behavior of high-temperature ferromagnetic phase transition of $SmMn_2Ge_2$ single crystal by modified Arrott plots and the Kouvel–Fisher method. The obtained critical exponents are between the long-range mean field model and short-range 3D magnetic models, suggesting the coexistence of multiple-range magnetic interactions in $SmMn_2Ge_2$, which is further proved by the interaction function $J(r) \sim r^{-4.68}$. The results

will provide more clues to understanding the complex magnetic structure in such compounds and further research. Our work reveals that the ternary rare-earth compounds are an attractive class of materials for both fundamental research and applications in the field of magnetism and spintronics.

Acknowledgments

This work was supported by the National Key Research and Development Program of China (Grant No. 2021YFA1600204), the Innovation Program for Quantum Science and Technology (Grant No. 2021ZD0302802), the National Natural Science Foundation of China (Grant Nos. U1832214, U2032213, 12104461, and 12074135), and the High Magnetic Field Laboratory of Anhui. Y. X. was supported by the Start-up Project of Anhui University (Grant No. S020318001/020).

References

[1] Steglich F, Aarts J, Bredl C D, Lieke W, Meschede D, Franz W and Schäfer H 1979 *Phys. Rev. Lett.* **43** 1892
[2] Kang J S, Allen J W, Gunnarsson O, Christensen N E, Andersen O K, Lassailly Y, Maple M B and Torikachvili M S 1990 *Phys. Rev. B* **41** 6610
[3] Custers J, Gegenwart P, Wilhelm H, Neumaier K, Tokiwa Y, Trovarelli O, Geibel C, Steglich F, Pépin C and Coleman P 2003 *Nature* **424** 524
[4] Welter R, Venturini G, Ressouche E and Malaman B 1995 *J. Alloys Compd.* **218** 204
[5] Kolmakova N P, Sidorenko A A and Levitin R Z 2002 *Low Temp. Phys.* **28** 653
[6] Hou Z, Li L, Liu C, Gao X, Ma Z, Zhou G, Peng Y, Yan M, Zhang X and Liu J 2021 *Mater. Today Phys.* **17** 100341
[7] Xu L, Bai Y, Gong G, Song F, Li Z, Han Y, Ling L and Tian Z 2022 *Phys. Rev. B* **105** 075108
[8] Zheng X, Zhao X, Qi J, Luo X, Ma S, Chen C, Zeng H, Yu G, Fang N, Rehman S U, Ren W, Li B and Zhong Z 2021 *Appl. Phys. Lett.* **118** 072402
[9] Fujii H, Okamoto T, Shigeoka T and Iwata N 1985 *Solid State Commun.* **53** 715
[10] Tomka G J, Ritter C, Riedi P C, Kapusta Cz and Kocemba W 1998 *Phys. Rev. B* **58** 6330
[11] Koyama K, Miura S, Okada H, Shigeoka T, Fujieda S, Fujita A, Fukamichi K and Watanabe K 2006 *J. Alloys Compd.* **408** 118
[12] Smart J S 1966 *Effective field theories of magnetism* (Philadelphia: Saunders)
[13] Santiago J M, Huang C and Morosan E 2017 *J. Phys.: Condens. Matter* **29** 373002
[14] Gyorgy E M, Batlogg B, Remeika J P, van Dover R B, Fleming R M, Bair H E, Espinosa G P, Cooper A S and Maines R G 1987 *J. Appl. Phys.* **61** 4237
[15] Zhang L 2018 *Acta Phys. Sin.* **6** 137501 (in Chinese)
[16] Arrott A and Noakes J E 1967 *Phys. Rev. Lett.* **19** 786
[17] Fisher M E 1967 *Rep. Prog. Phys.* **30** 615
[18] Fisher M E 1974 *Rev. Mod. Phys.* **46** 597
[19] Franco V, Blázquez J S and Conde A 2006 *Appl. Phys. Lett.* **89** 222512
[20] Pecharsky V K and Gschneidner Jr K A 1999 *J. Magn. Magn. Mater.* **200** 44
[21] Kadanoff L P 1966 *Phys. Phys. Fiz.* **2** 263
[22] Kouvel J S and Fisher M E 1964 *Phys. Rev.* **136** A1626
[23] Kaul S N 1985 *J. Magn. Magn. Mater.* **53** 5
[24] Huang K 1987 *Statistical Mechanics* (2nd edn.) (New York: Wiley)
[25] Fisher M E, Ma S and Nickel B G 1972 *Phys. Rev. Lett.* **29** 917
[26] Wang X, Wang W, Hutchison W, Wang C, Hao H, Su F, Xue Y, Debnath J, Campbell S, Cheng Z and Wang J 2022 *J. Alloys Compd.* **909** 164784
[27] Song M, Zhao J, Liu C, He M, Wang Y, Han Y, Ling L, Cao L, Zhang L, Qu Z and Xiong Y 2022 *Appl. Phys. Lett.* **120** 092402